



Numerical Simulation of Blood Flows in Patient-specific Abdominal Aorta with Primary Organs

Shanlin Qin¹ · Rongliang Chen^{1,3} · Bokai Wu¹ · Wen-Shin Shiu¹ · Xiao-Chuan Cai²

Received: 27 July 2020 / Accepted: 6 January 2021

© The Author(s), under exclusive licence to Springer-Verlag GmbH, DE part of Springer Nature 2021

Abstract

The abdominal aorta is the largest artery in the abdominal cavity that supplies blood flows to vital organs through the complex visceral arterial branches, including the celiac trunk (the liver, stomach, spleen, etc.), the renal arteries (the kidneys) and the superior and inferior mesenteric arteries (the small and large intestine, pancreas, etc.). An accurate simulation of blood flows in this network of arteries is important for the understanding of the hemodynamics in various organs of healthy and diseased patients, but the computational cost is very high. As a result, most researchers choose to focus on a portion of the artery or use a low-dimensional approximation of the artery. In the present work, we introduce a parallel algorithm for the modeling of pulsatile flows in the abdominal aorta with branches to the primary organs, and an organ-based two-level method for calculating the resistances for the outflow boundary conditions. With this highly parallel approach, the simulation of the blood flow for a cardiac cycle of the anatomically detailed aorta can be obtained within a few hours, and the blood distribution to organs including liver, spleen and kidneys are also computed with certain accuracy. Moreover, we discuss the significant hemodynamic differences resulted from the influence of the peripheral branches. In addition, we examine the accuracy of the results with respect to the mesh size and time-step size and show the high parallel scalability of the proposed algorithm with up to 3000 processor cores.

Keywords Computational hemodynamics · Blood flow simulations · Abdominal aorta with primary organs · Finite element · Parallel computing

1 Introduction

Human abdominal aorta supplies oxygen-rich blood to many vital organs, including the stomach, liver, kidneys, spleen, pancreas and intestines, among others. Vascular diseases occurred in the abdominal aorta can be life-threatening or even fatal, such as the abdominal aortic aneurysm (Chaikof et al. 2018; Kent 2014). The diagnosis and management of the vascular diseases are usually based on the geometric

morphology features, such as the size and shape, measured with imaging techniques or invasive operations. The accuracy of the diagnosis is sometimes limited; for example, some population-based studies report more than 50% inaccuracy in accessing the rupture risk by using the aneurismal maximum diameter (Chaikof et al. 2018; Ghulam et al. 2017). Combined with the medical image technologies, the numerical blood flow simulation has recently emerged as a promising tool to provide additional hemodynamic features for the diagnosis and treatment of vascular diseases (Taylor et al. 2013).

In recent years, many numerical techniques have been developed for the numerical simulation of the blood flow and can be summarized into two categories: the low-dimensional (0D, 1D and tube-load) and the high-dimensional (2D and 3D) methods (Grinberg et al. 2009; Liu et al. 2015; Zhou et al. 2019). The low-dimensional approaches are computationally inexpensive and capable of modeling the global circulation without concerning any detailed local fluid structures. The high-dimensional approach is more useful

✉ Xiao-Chuan Cai
xccai@um.edu.mo

Rongliang Chen
rl.chen@siat.ac.cn

¹ Shenzhen Institutes of Advanced Technology, Chinese Academy of Sciences, Shenzhen, China

² Department of Mathematics, University of Macau, Macau, China

³ Shenzhen Key Laboratory for Exascale Engineering and Scientific Computing, Shenzhen, China

to analyze the detailed local hemodynamics, that can be used to assist clinicians for the early diagnosis, risk assessment and treatment planning of the vascular diseases (Chisci et al. 2018; Chung and Cebal 2015). However, the high-dimensional approaches are computationally expensive and most of the existing works are restricted to low-resolution meshes or drastically simplified geometry (Boyd et al. 2016; Owen et al. 2016; Tse et al. 2011). Computational results in Blanco et al. (2020) address the significance of the aortic branches by directly comparing the anatomically detailed and simplified network vessels. Clinical findings in Ambler et al. (2015); Regnier et al. (2018) indicate that the flow changes in some peripheral branches caused by surgical interventions increase the organ-dysfunction risk. Therefore, in this paper, we focus on a highly efficient method capable of simulating blood flows in the abdominal aorta including the branches of the primary organs.

We now briefly review some works that consider the side branches during the 3D blood flow simulation in the abdominal aorta. For hypothetical aortic geometries, the steady flow was studied in tubes with four (Shipkowitz et al. 1998, 2000) and seven branches (Lee and Chen 2003; Taylor et al. 1998). The pulsatile flow was simulated in four-branch geometric models with different anatomic variations (Kandail et al. 2015). Recently in Xiong et al. (2016); Li et al. (2018), the local patterns of the blood flow generated by hypothetical graft implantations were investigated in a tube with a renal branch. For patient-specific geometries, there is a trend of utilizing more realistic geometries with increasing number of branches. Initially, most researchers focused on tube-like structures with one bifurcating branch. Later in Frauenfelder et al. (2006), several branches were included to study the blood flow changes caused by stent-graft implantations. In Les et al. (2010), the hemodynamic difference in a ten-branch abdominal aorta was studied for the scenarios of resting and exercising. We mention that some rather large simulations of full-body arterial networks were conducted in Figueroa and Humphrey (2014); Xiao (2014), but there is no clinical verification for the computed results (Zhou et al. 2010). Despite a large number of publications on blood flow simulations, 3D simulations with a complex network of arterial branches are still scarce in the literature since the number and geometric complexity of the aortic branch dramatically increase the computational cost, the memory requirement, and the difficulties of solving the partial differential equations. In order to meet the computational requirement, parallel algorithms implemented on supercomputers are essential for a large-scale imaged-based CFD blood flow simulation. Therefore, in this paper, we adopt a highly parallel framework to study the influence of the primary and peripheral branches on the local hemodynamics of the abdominal aorta.

To obtain an accurate assessment of the blood flow distribution from the aorta to specific organs or regions is another point to be considered in this paper. Different approaches have been proposed via the adjustment of the terminal resistance to achieve a desired blood flow distribution. For example, the commonly used Murray's law relates the flow rate to the diameter of the vessels (Luo et al. 2019; Taylor et al. 2013). Though the resulting flow rate is inversely proportional to the vessel size, this approach does not guarantee a required blood supply to specific destinations. In Grinberg and Karniadakis (2008), clinically measured flow rates are imposed to the cranial arteries with ten outlets through the use of a time-dependent resistance. However, it is infeasible to measure the flow rates for all outlets of a complex geometrical model such as the one under consideration in the present paper. In Blanco et al. (2012, 2014), the adjustment of the blood flow was equivalently transformed into an optimization problem of setting optimal values for the terminal resistances, but it was implemented only for the one-dimensional case. The importance of a desired blood supply to a specific organ is well recognized, but not often considered during the simulation due to its high computational cost and complexity in the implementation. In this paper, we introduce a resistance-flow relationship that can approximately achieve a given blood flow distribution without increasing much of the overall computational cost.

The computational task is very challenging and requires an algorithm that is highly scalable, and also robust with respect to the complex configuration of the arterial network and the associated flow parameters. Therefore, we adopt the Newton–Krylov–Schwarz (NKS) framework to solve the large-scale, sparse and nonlinear system incurred by the discretization of the governing equations. Literally, the NKS utilizes an inexact Newton method to deal with the nonlinearity of the system and a Krylov subspace method to solve the Schwarz preconditioned linear Jacobian system within each Newton step (Luo et al. 2019). The NKS has been successfully applied to many different problems, such as the fluid flow modeling (Luo et al. 2019), the atmospheric transport simulation (Yang and Cai 2014) and the aerodynamic analysis (Liao et al. 2019). Its parallel scalability with application to the blood flow modeling has been studied in Kong et al. (2018), without the consideration of the Windkessel outlet boundary condition, which requires more communications among subdomains due to its integral nature.

The rest of this paper is organized as follows. In Sect. 2, we first give a description of the abdominal aorta with branches of the primary organs and introduce the meshing of the artery and then present the numerical method to solve the governing equations with the Windkessel boundary condition. In Sect. 3, a patient-specific abdominal aorta is studied and analyzed with an emphasis on the hemodynamic changes due to the influence of the branches and the

organ-based blood flow distributions. We also discuss the numerical properties of the method including the accuracy of the solution and the scalability of the algorithm. Finally, we draw some conclusions in Sect. 4.

2 Methodology

2.1 Image segmentation and meshing

As shown in Fig. 1, we consider a patient-specific abdominal aorta with 144 outlet branches, including several closed loops of the interconnected arteries. All primary branches are marked in the figure, including the celiac artery (to the liver, stomach, spleen, etc.), the renal arteries (to the two kidneys), the superior and inferior mesenteric arteries (to the small and large intestine, pancreas, etc.), the inferior phrenic arteries (to the diaphragm), the middle suprarenal arteries (to the suprarenal glands) and the iliac arteries (to lower limbs). The geometry is reconstructed from a computed tomography angiography (CTA) image by using a region growth method in the Mimics (Materialise, Leuven, Belgium). The minimum outlet diameter is 0.93 mm, and the pixel spacing of the used CTA image is 0.68 mm. To have a more reliable segmentation, we perform manual corrections in the Geomagic Studio (Geomagic, Morrisville, North Carolina). Since we are also interested in computing the flow distribution to specific organs, vessels connected to the interested organs are grouped together, including the proper hepatic artery (yellow) to the liver, the splenic artery (green) to the spleen, the left (blue) and right (purple) renal arteries to the left and right kidneys.



Fig. 1 The 3D geometry of human abdominal aorta with 144 branches reconstructed from CT images. Major branches are marked, including the proper hepatic artery (yellow) to the liver, the splenic artery (green) to the spleen, the left (blue) and right (purple) renal arteries to the kidneys

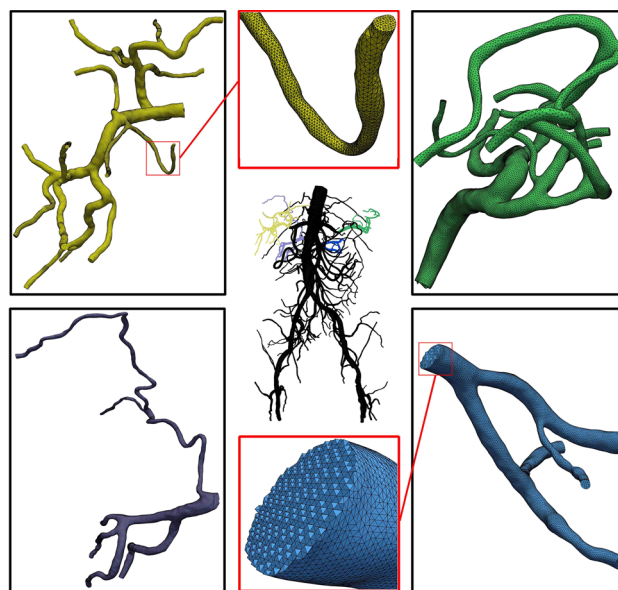
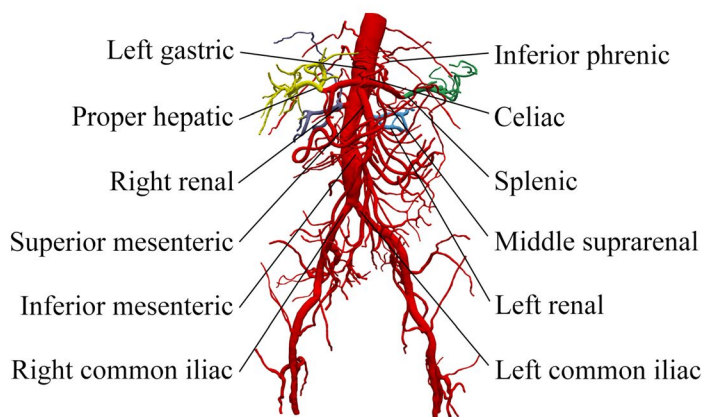


Fig. 2 A schematic diagram of a coarse mesh for the abdominal aorta. Meshes for branches of target organs including the liver, the spleen and the left and right kidneys are shown in magnified images. Noted that some of the peripheral branches cannot be segmented due to the limited CT resolution

We denote the artery as Ω , with one inlet Γ_I , m outlets Γ_O^i ($i = 1, 2, \dots, m$) and the wall surface Γ_w . An unstructured tetrahedral mesh is generated to cover Ω by using the ICEM (ANSYS, Canonsburg, Pennsylvania). A schematic diagram of a coarse mesh is shown in Fig. 2. The mesh is highly non-uniform with smaller elements in smaller branches and the diameters of the elements range from less than a millimeter to several millimeters. For some part of the artery, the mesh size is manually adjusted. In Fig. 2, magnified images in black boxes show the coarse



meshes of the arteries to specific organs, and those in red boxes show the locally refined meshes. Note that the coarse meshes are used for display only and not for actual computations. The whole process takes a few hours for a user with enough experiences using the segmentation and meshing software.

2.2 Governing equations and boundary conditions

The blood flow is considered as an incompressible Newtonian fluid and governed by the following 3D Navier–Stokes equations (Morris et al. 2016),

$$\begin{aligned} \rho \left(\frac{\partial \mathbf{u}}{\partial t} + (\mathbf{u} \cdot \nabla) \mathbf{u} \right) - \nabla \cdot \boldsymbol{\sigma} &= 0, \quad \text{in } \Omega \times (0, T], \\ \nabla \cdot \mathbf{u} &= 0, \quad \text{in } \Omega \times (0, T], \end{aligned} \tag{1}$$

where ρ is the fluid density; $\boldsymbol{\sigma} = -p\mathbf{I} + \mu(\nabla\mathbf{u} + \nabla\mathbf{u}^T)$ is the Cauchy stress tensor with \mathbf{I} being a 3×3 identity matrix and μ being the fluid dynamic viscosity; p is the pressure and \mathbf{u} is the velocity vector with 3 components.

The solution of (1) is determined by the initial and boundary conditions. Since there is no realistic initial condition available, we begin our calculation with zero velocity and zero pressure. The Dirichlet boundary condition is prescribed to the inlet boundary, which takes the form

$$\mathbf{u} = \mathbf{v}_I, \quad \text{on } \Gamma_I \times (0, T], \tag{2}$$

where \mathbf{v}_I is the inflow velocity and can be derived by the relationship $\mathbf{v}_I = \mathbf{n} \cdot Q/S$, where S and \mathbf{n} are the area and the inward normal of the inlet, and Q is a given inflow rate profile. The rigid no-slip boundary condition is applied to the wall boundary as

$$\mathbf{u} = 0, \quad \text{on } \Gamma_W \times (0, T]. \tag{3}$$

The 3-element Windkessel model is applied as the boundary condition to all the outlets, as shown in Fig. 3 for the i^{th} outlet. The model is based on a proximal resistance R_i^1 in series with a component consisting of a resistance R_i^2 in parallel with a capacitor C_i , accounting for the resistance and compliance at the downstream vasculature, respectively. Let $p_i'(t)$ be the distal pressure at the i^{th} outlet, then the corresponding outlet boundary pressure $p_i(t)$ and flow rate $Q_i(t)$ are related by the following relationship (Capoccia 2015; Vignon-Clementel et al. 2006)

$$\begin{aligned} p_i(t) &= p_i'(t) + \left(p_i(0) - p_i'(0) - R_i^1 Q_i(0) \right) e^{-t/\tau_i} \\ &\quad + R_i^1 Q_i(t) + \int_0^t \frac{e^{-(t-s)/\tau_i}}{C_i} Q_i(s) ds, \\ \tau_i &= R_i^2 C_i, \quad i = 1, 2, \dots, m, \end{aligned} \tag{4}$$

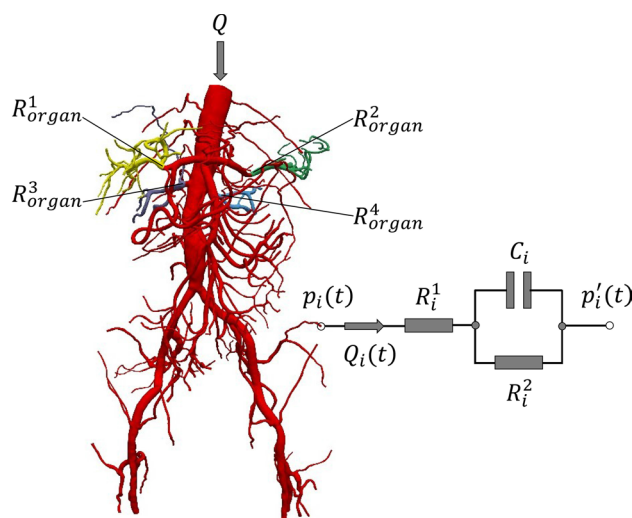


Fig. 3 The inlet and outlet boundary conditions. The inlet velocity boundary condition is obtained from the inlet flow rate Q . R^k_{organ} with $k = 1, 2, 3$ and 4 represent the total organ resistances to the liver, the spleen, the right and left kidneys, respectively. The three-element Windkessel model is applied at the boundary of each outlet

where Q_i takes the form $Q_i = \int_{\Gamma_i} \mathbf{u} \cdot \mathbf{n}_i d\Gamma$ with \mathbf{n}_i being the outward surface normal at the i^{th} outlet; $p_i(0)$ and $Q_i(0)$ are the initial pressure and flow rate at the outlet, respectively. In this paper, we set the distal pressure $p_i'(t)$ and its initial value $p_i'(0)$ to be 0, as suggested in Liu et al. (2017); Zhang et al. (2009).

2.3 Two-level outlet resistance distributions

The total capacitance C_T and resistance R_T are needed in order to determine the capacitance C_i and resistance R_i^1 and R_i^2 in (4) for all the outlets. For this purpose, we consider a Windkessel model at the inlet and the patient-specific C_T and R_T are chosen with the given values of the diastolic and systolic pressures of the patient (Xiao et al. 2014). The way to split C_T and R_T to the outlets directly affects the results of the simulation. Usually, for an artery with multiple outlets, the capacitance and the resistance of the i^{th} outlet are distributed according to the radii of the branch outlet surface by

$$C_i = C_T r_i^2 \left(\sum_{l=1}^m r_l^2 \right)^{-1}, \tag{5}$$

$$R_i = R_T (r_i^3)^{-1} \sum_{l=1}^m r_l^3, \tag{6}$$

where r_l is the radius of the l^{th} outlet (Fossan et al. 2018; Lan et al. 2018). However, when the complexity of the artery increases to include artery trees to multiple organs, this

approach fails to provide a reasonable estimate of the flow distributions to these organs (Blanco et al. 2012). To quantify the blood flow distribution to specific organs, we define the following blood flow fraction

$$F_{organ}^k = \bar{Q}_{organ}^k / \bar{Q}, \quad (7)$$

where \bar{Q}_k is the total blood flow entering the inlet in a cardiac cycle, \bar{Q}_{organ}^k is the total blood flow exiting k^{th} organ. According to the clinical reference values published in Valentin (2002), when the cardiac output is given, the blood flow fraction of the organs should be 6.50% for the liver, 3.00% the spleen and 9.50% for both the left and right kidneys, as shown in the second column of Table 1. However, if we apply the rule (6), with our calculation, the blood flow fraction of the organs is very different and is clearly wrong as shown in the third column of Table 1. Therefore, to meet a required blood supply to specific organs, we introduce a different rule to split the resistance.

Following Grinberg and Karniadakis (2008), for each outlet the resistance R_i and the flow rate \bar{Q}_i satisfy the following relationship approximately

$$\bar{Q}_i R_i = R_T \bar{Q}. \quad (8)$$

As presented in Grinberg and Karniadakis (2008), the error of (8) is influenced by the value of terminal resistance, vessel length, nonlinear effect and 3D geometry of the model, but in practice, the error is small enough that can be ignored since the value of terminal resistance is sufficiently large.

(8) can be used to derive the resistance R_i if the corresponding \bar{Q}_i is available. Unfortunately, \bar{Q}_i is generally not available for each individual outlet. In the present work, we introduce a two-level resistance distribution algorithm that first splits the total resistance to different organs using (8) and then further split the organ resistance to each individual outlet using (6). Let R_{organ}^k be the total resistance of the k^{th} organ as shown in Fig 3, then following (8), we have

$$R_{organ}^k \bar{Q}_{organ}^k = R_T \bar{Q}. \quad (9)$$

Table 1 The blood flow fractions to specific organs, including the liver, the spleen and the left and right kidneys. The second column is the clinically measured blood flow fraction reported in Valentin (2002). The third column is the computed blood flow fraction when the resistance is split by (6)

Arteries	Measured	Computed
Proper hepatic	6.50%	2.77%
Splenic	3.00%	1.75%
Left renal	9.50%	5.53%
Right renal	9.50%	2.21%

Since the blood flow fractions to individual organs are clinically available, R_{organ}^k can be solved from (9) for each organ. The resistance for each outlet of this organ can be computed using (6) with R_T replaced by R_{organ}^k . The resistance of other outlets not belong to the organs can be calculated using (6) directly. After obtaining R_i for all outlets, the resistances within the Windkessel model of the i^{th} outlet are then calculated by the relationship $R_i = R_i^1 + R_i^2$ with $R_i^1 = 0.055R_i^2$ (Blanco et al. 2014).

2.4 Numerical methods

The blood flow model described in (1) is discretized by an implicit backward Euler method in time and a stabilized $P_1 - P_1$ (linear velocity and pressure) finite element method in space. The stabilization term is added since the $P_1 - P_1$ pair does not satisfy the inf-sup or Ladyzhenskaya–Babuška–Brezzi condition. The detail of discretization can be found in Kong et al. (2018). The discretization leads to a sequence of large, sparse and nonlinear algebraic system to be solved at each time step,

$$\mathcal{F}(\mathcal{X}) = 0. \quad (10)$$

Because of the fine mesh required to ensure the accuracy of the solution, the size of the system (10) is very large. Moreover, due to the complex nature of the geometry, the solution changes drastically in time and in space, therefore a highly parallel and sufficiently robust method is required to solve (10). We adopt the class of domain decomposition methods called Newton–Krylov–Schwarz (NKS) which solves the nonlinear system (10) with an inexact Newton method, and the Jacobian problems in the Newton method are solved by a Krylov subspace method preconditioned by a Schwarz type overlapping domain decomposition method. Specifically, for each time step, this algorithm obtains a new approximate solution \mathcal{X}_{k+1} by updating the previous solution \mathcal{X}_k along the Newton direction S_k with a step length λ_k

$$\mathcal{X}_{k+1} = \mathcal{X}_k + \lambda_k S_k, \quad (11)$$

until a given absolute or relative tolerance is reached. In this formula, the step size λ_k is calculated by a cubic line-search method and the Newton correction S_k is obtained by solving the following preconditioned Jacobian system

$$J_k M_k^{-1} M_k S_k = -\mathcal{F}(\mathcal{X}_k), \quad (12)$$

where M_k^{-1} is the restricted additive Schwarz preconditioner; J_k is the Jacobian matrix of $\mathcal{F}(\mathcal{X})$ which is analytically computed to provide the required robustness and to reduce the overall compute time (Barker and Cai 2010). We solve (12)

approximately using the Krylov subspace method, GMRES, to satisfy

$$\|J_k M_k^{-1} M_k S_k + \mathcal{F}(\mathcal{X}_k)\| \leq \eta_k \|\mathcal{F}(\mathcal{X}_k)\|, \quad (13)$$

where the forcing term η_k is used to control the accuracy for the linear solver.

3 Results and discussions

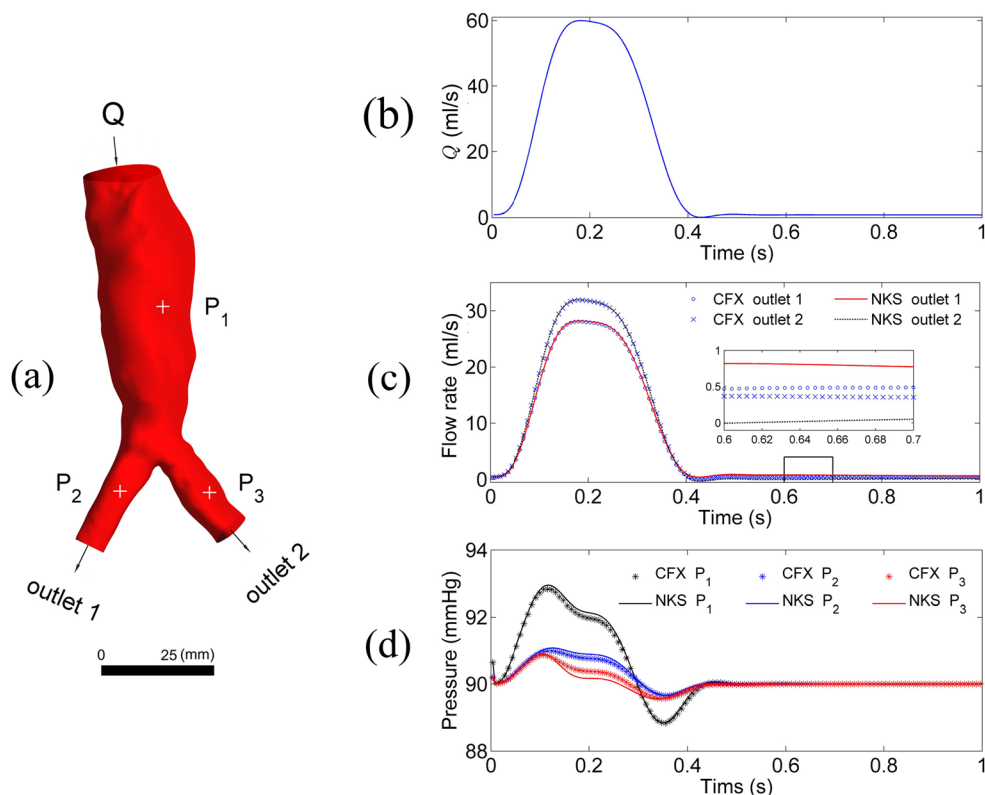
In this section, we first present a validation of the proposed numerical method by comparing our computed solution with that obtained with the commercial software CFX (ANSYS, Canonsburg, Pennsylvania). Then, we focus on the simulation of blood flows in a patient-specific aorta with primary organs. Last, we study some properties of the proposed algorithm. Our method is implemented on top of the open source software package Portable Extensible Toolkit for Scientific computing (PETSc) library (Balay et al. 2020). The blood flow is characterized with a density of $\rho = 1.06 \text{ g/cm}^3$ and a dynamic viscosity of $\mu = 0.035 \text{ g/cm s}$. For the NKS solver, the inexact Newton iteration is stopped with the relative or absolute tolerance 10^{-6} and the Krylov iteration is stopped by the relative tolerance 10^{-3} .

3.1 A benchmark problem

To validate the proposed method, we consider the simulation of blood flow in a relatively simple geometry and compare the results with that obtained with CFX. As shown in Fig. 4a, we consider a patient-specific abdominal aorta bifurcating into two iliac vessels. Three monitor points are placed on the surface at which we compare the computed values from different methods. A constant pressure of 90 mmHg is imposed as the outlet boundary conditions. A patient-specific inflow boundary condition is prescribed with a flow rate Q given in Fig. 4b. For the CFX-based simulation, the conservation equations for the mass and momentum are solved by using a backward Euler scheme in time and a finite volume method in space. The simulation is carried out for a full cardiac cycle on 16 CPU cores, and its convergence is achieved when the root mean square residual reaches 10^{-4} . For the NKS-based simulation, 240 CPU cores are used. For both simulations, we use the same mesh with 970025 tetrahedral elements and the time-step size is 0.004 s.

As shown in Fig. 4c, the computed flow rates at the two outlets obtained from NKS and CFX agree quite well. Both methods observe a greater flow at outlet 2 than outlet 1 in the earlier phase of the cardiac cycle; later in the cycle more flow exits outlet 1 than outlet 2, see the magnified image in Fig. 4c. Fig. 4d depicts the temporal variation of the pressure at the three monitor points. It can be seen that both methods

Fig. 4 A benchmark comparison between NKS and CFX: **a** the computational domain is the abdominal aorta with two outlets; **b** a pulsatile flow is imposed on the inlet boundary; **c** the comparison of the temporal evolution of the flow rates at two outlets and **d** the pressures at three monitor points computed with NKS and CFX



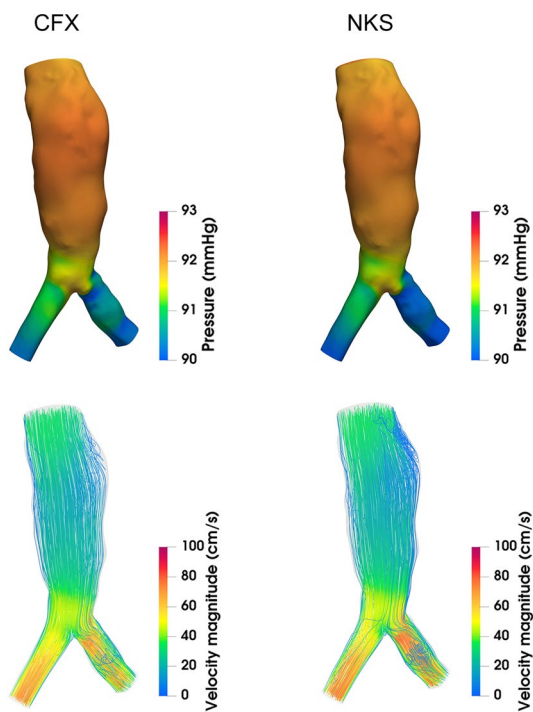


Fig. 5 The pressure and velocity distributions at $t = 0.2$ s computed with NKS and CFX

yield well-consistent results for the temporal evolution of the pressures, with a root mean-square error 0.06 mmHg for P_1 , 0.05 mmHg for P_2 and 0.08 mmHg for P_3 .

We also compare the spatial distributions of the pressure and velocity at $t = 0.2$ s in Fig. 5. For the pressure, although minor pressure differences exist at the location near the outlet 2, similar distributions are obtained by both methods, with relatively higher values on the surface of the abdominal aorta and lower values on the surface of the branches. For the velocity, though slight differences exist in the location where the pressure differs, similar contours are obtained by both methods, with relatively higher values in the branches and lower values in the abdominal aorta. Overall, the results are well matched, which validates the correctness of the proposed numerical algorithm.

3.2 Abdominal aorta with major organs

In this subsection, we consider an abdominal aorta with branches to major organs in the abdominal cavity (see Fig. 1). There are 144 outlets, including 16 in the liver, 9 in the spleen, 4 in the left kidney and 6 in the right kidney. To compare our results with those from the Blanco's work (Blanco et al. 2014), we extract its flow rate profile at the suprarenal location of the abdominal aorta as our inlet boundary condition, as shown in Fig. 6. The flow rate is scaled by a factor of 0.74, which is derived by scaling

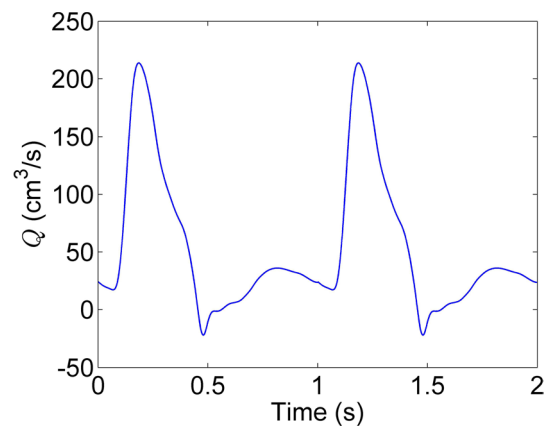


Fig. 6 The inflow rate profile for two cardiac cycles is imposed as the inlet boundary condition

down the cardiac output from 6.727 L/min to a standard value of 5.00 L/min (Zhang et al. 2015). Let D be the diameter of the inlet, then the Reynolds number can be estimated by $Re = \rho u D / \mu$ with a peak value 3499 at the inlet. Note that, in Blanco et al. (2014), the cardiac output is 6.727 L/min, among which 4.37 L/min goes to the abdominal aorta, accounting for 65.00% of the cardiac output. The same percentage is maintained in our study so that 3.25 L/min goes to the abdominal aorta amidst the cardiac output 5.00 L/min. The initial pressures for the inlet and the i^{th} outlet in the Windkessel model, namely $p(0)$ and $p_i(0)$, are all set to 91.00 mmHg. The mesh consists of 14272020 tetrahedral elements and 2802677 nodes. The average length of the minimum element edge is about 0.30 mm, which is smaller than the spatial resolution 0.68 mm of the CTA image. To reach a periodic state, the simulation is carried out for two cardiac cycles. The time-step size is 0.001 s. The overall computation takes about 21 hours of wall clock time with 1080 processor cores.

Using the diastolic pressure 91.00 mmHg and the systolic pressures 136.00 mmHg at the abdominal aorta from Blanco et al. (2014), the total resistance R_T and the total compliance C_T are 2680.97 dyn · s/cm⁵ and 4.16×10^{-4} cm⁵/dyn, respectively. Table 2 lists the resistance and the blood flow fraction obtained with and without the use of the organ-based resistance R_{organ}^k . Without using the intermediate level of resistance R_{organ}^k , as pointed out in Table 1, the computed blood flow fractions to interested organs, including the liver, the spleen and the left and right kidneys, are far from the clinically measured values in Valentin (2002).

By introducing the total resistances to the organs, we can regulate the blood flow to the organs. As shown in Table 2, the computed blood flow fractions are 6.42% for the proper hepatic artery, 3.03% for the splenic artery, 9.61% and 9.25% for the left and right renal arteries. We quantify the

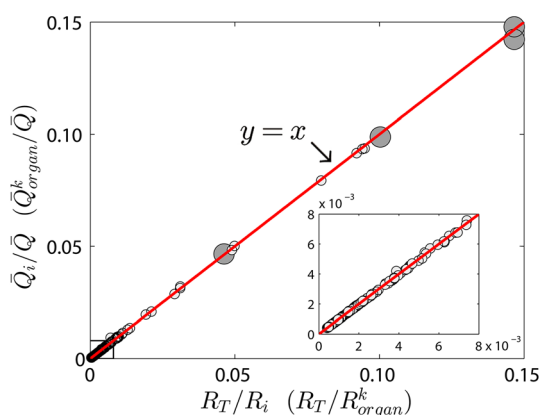


Fig. 7 A near equality of the blood flow fraction \bar{Q}_i/\bar{Q} ($\bar{Q}_{organ}^k/\bar{Q}$) and the ratio of resistance R_T/R_i (R_T/R_{organ}^k) for 144 outlets (small circle) and 4 organs (large circle)

discrepancy between the computed blood flow fraction and the clinically measured one by calculating the relative errors

$$e_1 = \frac{|F_{organ}^k(\text{measured}) - F_{organ}^k(6)|}{F_{organ}^k(\text{measured})},$$

$$e_2 = \frac{|F_{organ}^k(\text{measured}) - F_{organ}^k(\text{new})|}{F_{organ}^k(\text{measured})}, \tag{14}$$

where $F_{organ}^k(\text{measured})$ is the clinically measured blood flow fraction reported in Valentin (2002); $F_{organ}^k(6)$ and $F_{organ}^k(\text{new})$ are the computed blood flow fractions obtained without and with the use of total resistances to the organs,

Table 2 The resistance and the blood flow fraction to specific organs, including the liver, the spleen and the left and right kidneys. “NA” is the number of arteries to the target organs; “ $F_{organ}^k(\text{measured})$ ” is the clinically measured blood flow fraction reported in Valentin (2002); “ $R_{organ}^k(6)$ ”, “ $F_{organ}^k(6)$ ” and e_1 are the resistance to each organ, the

Arteries	NA	$F_{organ}^k(\text{measured})$	$R_{organ}^k(6)$	$F_{organ}^k(6)$	e_1	$R_{organ}^k(\text{new})$	$F_{organ}^k(\text{new})$	e_2
Proper hepatic	16	6.50%	62755.61	2.77%	57.38%	26727.23	6.42%	1.23%
Splenic	9	3.00%	99693.75	1.75 %	41.67%	57909.00	3.03%	0.01%
Left renal	4	9.50%	32049.87	5.53%	41.81%	18287.05	9.61%	1.16%
Right renal	6	9.50%	81896.10	2.21%	76.74%	18287.05	9.25%	2.63%
Others	109	–	3293.57	52.87%	–	4785.87	36.81%	–
Total	144	–	2681.00	65.13%	–	2681.00	65.12%	–

Table 3 Comparison of the flow rate between our computed and the clinically measured data from publications

Arteries	Measured (ml/min)	Computed (ml/min)
Proper hepatic	337 ± 204, 215 ± 101 (Yzet et al. 2010)	321.2
Splenic	179 ± 37 (Sato et al. 1987), 370 ± 181 (Nakamura et al. 1989)	151.7
Left/right renal	413 ± 122 (Keegan et al. 2015)	480.4/462.7

respectively. It shows that the accuracy in the estimation of the flow to organs is greatly improved by the use of the organ-based resistance. Moreover, the total output volumes are consistent with the input volume over the cardiac period, accounting for 65.00% of the cardiac output, which strictly satisfies the mass conservation no matter how the resistance is distributed. We remark that though allocated with the same value of resistance, the obtained blood flow fractions are not exactly the same here for the two renal arteries, which may be due to the geometrical difference, as has been reported in Lee and Chen (2002). We also compare the computed flow rates to the individual organs with the published data in Table 3 and they agree well. By using the total resistance R_T and the total flow \bar{Q} , we compute two flow fractions and ratios of resistance. In the first level, namely the organ level, using the values of R_{organ}^k and Q_{organ}^k for each of the organs, we compute the ratios R_T/R_{organ}^k and $\bar{Q}_{organ}^k/\bar{Q}$. In the second level, using the values of R_i and \bar{Q}_i for each of the outlets, we compute the ratios R_T/R_i and \bar{Q}_i/\bar{Q} . We then plot the two levels of blood flow fractions and ratios of resistance in Fig. 7. It shows a near equal relationship for both levels, which verifies the correct implementation of (9).

Fig. 8 plots the temporal evolution of the flow rates of the interested organs and the pressure at four monitor points, P_a, P_b, P_c and P_d , obtained with and without the use of the organ-based resistance. “One-level pressure” and “One-level flowrate,” represented by the dotted lines, are the pressure and flow rate calculated when all the resistance are split by (6). “Two-level pressure” and “Two-level flowrate,” represented by the solid lines, are the pressure and flow rate calculated when the organ-based resistance is applied before

obtained blood flow fraction and the relative errors when the terminal resistance is split directly by (6). “ $R_{organ}^k(\text{new})$ ”, “ $F_{organ}^k(\text{new})$ ” and e_2 are their counterparts obtained when the organ-based resistance R_{organ}^k is applied

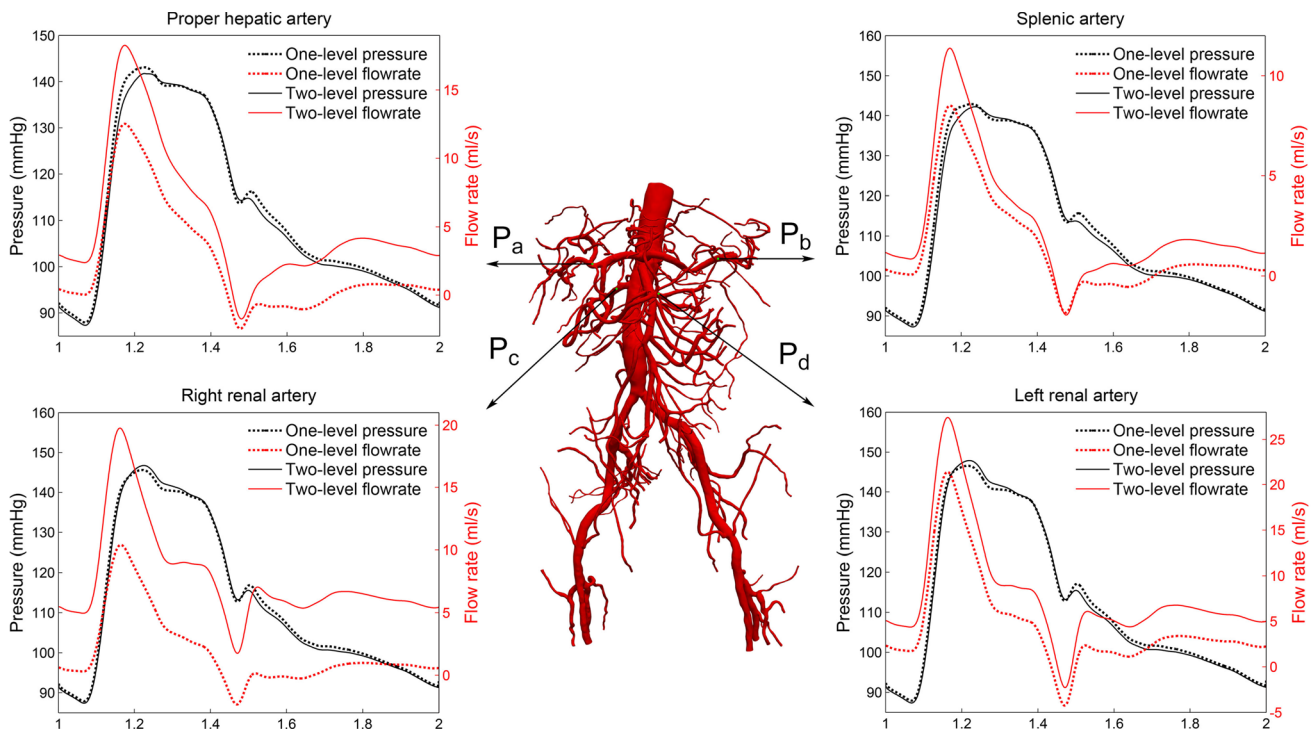


Fig. 8 A comparison of the pressures at four monitor points (P_a , P_b , P_c and P_d) and flow rates to the liver, the spleen and the left and right kidneys, obtained with and without the organ-based resistance. “One-level pressure” and “One-level flowrate” are the pressure and

flow rate obtained when all the terminal resistances are split by (6). “Two-level pressure” and “Two-level flowrate” are their counterparts obtained with the organ-based resistance

the split by (6). It shows that the organ-based resistance has a significant impact on the magnitude of the flow rate. More specifically, by decreasing the organ-based resistance from R_{organ}^k (6) to R_{organ}^k (new) as in Table 2, the percentages of flows to these organs are increased in “Two-level flowrate” comparing to “One-level flowrate,” thus closer to the clinically measured values. The maximum increment of the flow rates is 5.75 ml/s, 2.87 ml/s, 6.03 ml/s and 9.41 ml/s for the proper hepatic artery, the splenic artery and the left and right renal arteries, respectively. It also changes the pressure profile with maximum differences of 4.27 mmHg, 4.36 mmHg, 2.30 mmHg and 2.15 mmHg for P_a , P_b , P_c and P_d , respectively. Comparing with the results in Blanco et al. (2014), the profiles of the pressure and the flow rate show roughly the same fluctuations but with different amplitude and local oscillations. This may due to the interindividual variability of the geometry, the inclusion of closed arterial loops, the use of 3D mathematical model vs. 1D model in Blanco et al. (2014), or the lack of compliance in the arterial wall of our model. It is reported that the compliance of the arterial wall affects the blood flow pulsatility and dampens the amplitude of fluctuations in the pressure and the flow (Lefferts et al. 2014).

Fig. 9 shows the spatial distribution of the pressure in the abdominal aorta and the proper hepatic artery at $t = 1.2$ s.

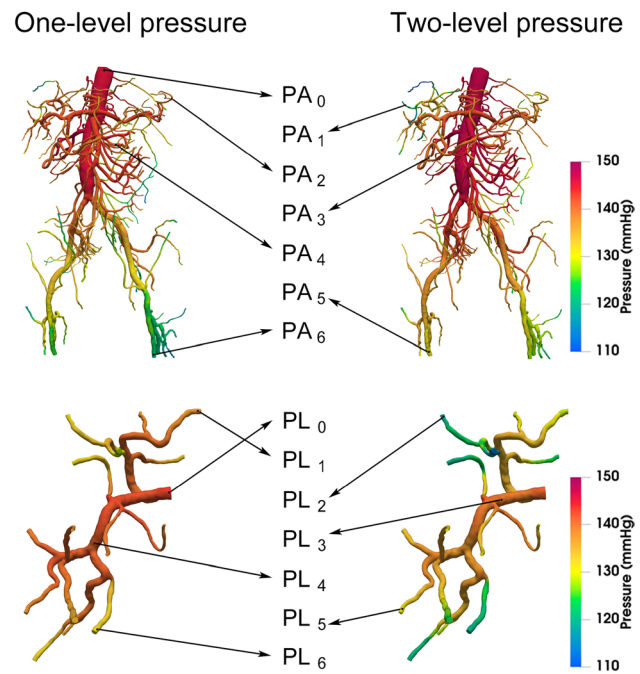


Fig. 9 The pressure distribution in the abdominal aorta and the proper hepatic artery at $t = 1.2$ s. Selected points PA_i and PL_i ($i = 0, 1, \dots, 6$) are labeled in the abdominal aorta and the proper hepatic artery, respectively, for a quantitative analysis

As has been described, “One-level pressure” and “Two-level pressure” are the pressures calculated without and with the organ-based resistance, respectively. It can be seen that both “One-level pressure” and “Two-level pressure” show gradual decreases from proximal to distal at this moment, but the specific nodal values are different. Comparing to “One-level pressure”, “Two-level pressure” shows lower pressure values in the branches of the four organs where the terminal resistances are reduced and higher pressure values at other branches where the terminal resistances are increased (see Table 2 for the value of the resistance). This trend can be quantitatively described by the pressure values at the selected points PA_i in the abdominal aorta and PL_i in the proper hepatic artery ($i = 0, 1, \dots, 6$), as shown in Table 4. In the abdominal aorta, “Two-level pressure” has smaller values at the monitor points PA_1 , PA_2 , PA_3 and PA_4 , and larger values at PA_0 , PA_5 and PA_6 , comparing to those values in “One-level pressure.” Consequently, by considering the organ-based resistance, pressure drops increase at PA_1 , PA_2 , PA_3 and PA_4 and decrease at PA_5 and PA_6 with respect to the pressure at PA_0 . In the proper hepatic artery, the pressure values at all monitor points in “Two-level pressure” decrease due to the reduced terminal resistance comparing with the values in “One-level pressure.” Although the pressure at PL_0 decreases in “Two-level pressure” as well due to the organ-based resistance, the pressure drops at all monitor points increase comparing with those in “One-level pressure.” Therefore, the flow rate to a specific outlet can be proportionally regulated according to the pressure drop.

3.3 The influence of peripheral branches

The computational cost increases a lot when the arterial tree has many branches. Many publications choose a small subset of branches to reduce the cost. In this section, we compare these two approaches. The blood flow in the abdominal aorta with different number of outlets is compared to study the

influence of the branches. In the original complex artery tree (Fig. 1) that we segmented from the CT image, there are 144 outlets, and a simpler model with 18 outlets (the right picture in Fig. 11) is generated, with 2 arteries in the liver, 3 arteries in the spleen and 2 arteries in each kidney. A mesh consisting of 8463732 tetrahedral elements and 1513269 nodes is used for the computation. Using the same values of the organ-specific resistances listed in Table 2, the computed blood flow fractions are 6.47% for the liver, 2.99% for the spleen and 9.46% for the left and 9.45% for the right kidneys. The results are quite close to the fractions computed with the larger 144-outlets artery tree as shown in Table 2. Even though we obtain almost the same values of blood flow fractions for the left and right renal arteries, the flow rate profiles are not exactly the same, shown as “Left-18” and “Right-18” in Fig. 10. They also present some differences comparing with the flow rate computed with the more complex artery tree with 144 outlets obtained in the previous subsection, shown as “Left-144” and “Right-144” here. The discrepancy in the profile of renal flow rates can be explained by the different values of the terminal parameters in the outlet boundary condition, due to the redistribution of the total compliance and the organ-level resistance as a result of the

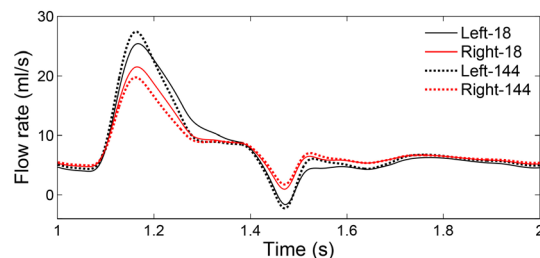


Fig. 10 A comparison between the flow rate of two renal arteries calculated based on the abdominal aorta with 144 and 18 branch outlets. “Left-18” and “Right-18” represent the case of 18 outlets. “Left-144” and “Right-144” represent the case of 144 outlets

Table 4 The pressure values at selected monitor points in the abdominal aorta PA_i and the proper hepatic artery PL_i ($i=0,1,2,\dots,6$) at $t = 1.2$ s. ΔP_1 and ΔP_2 are the pressure drops, with respect to the

	PA_0	PA_1	PA_2	PA_3	PA_4	PA_5	PA_6
One-level pressure	145.63	132.18	139.68	141.05	140.99	124.92	121.61
Two-level pressure	147.58	120.53	136.09	129.16	138.59	130.60	127.62
ΔP_1	–	13.45	5.96	4.58	4.64	20.71	24.02
ΔP_2	–	27.05	11.49	18.42	8.99	16.98	19.96
	PL_0	PL_1	PL_2	PL_3	PL_4	PL_5	PL_6
One-level pressure	142.91	136.54	131.15	141.98	140.86	137.36	131.73
Two-level pressure	140.72	128.15	118.69	139.39	137.06	129.99	119.72
ΔP_1	–	6.37	11.76	0.93	2.05	5.55	11.18
ΔP_2	–	12.57	22.03	1.33	3.66	10.73	21.00

proximal points PA_0 and PL_0 , when the resistance is split without and with the organ-based resistance, respectively

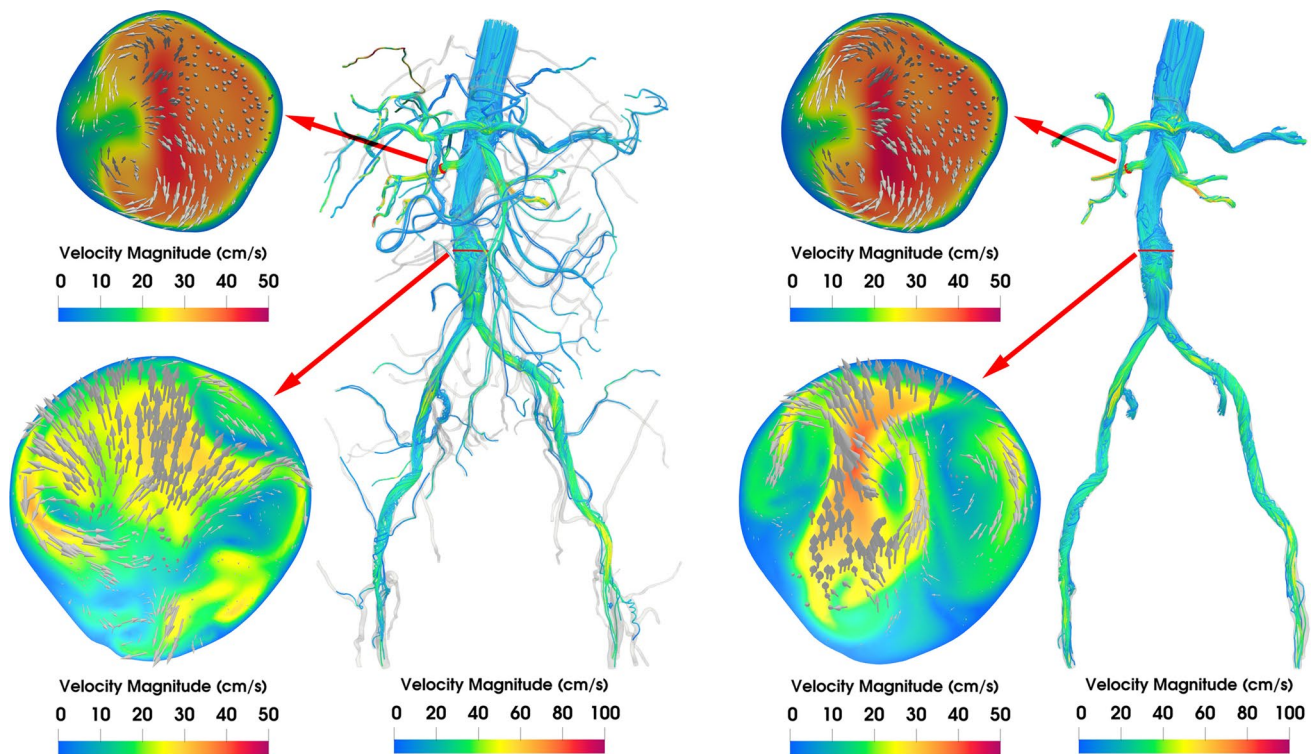


Fig. 11 The instantaneous streamline of the whole velocity field and the velocities extracted along 2D slices for the right renal artery and the abdominal aorta with 144 and 18 outlets at $t = 1.4$ s. The velocity vectors in the slices are represented by the arrows

truncation of the arterial network. The difference in the flow rate between the complex and simpler geometrical models has also been demonstrated in the one-dimensional simulation of the recent work (Blanco et al. 2020).

To see the influence of the peripheral branch on the hemodynamics, we show the differences between the complex and simpler models both in time and in space. For the monitor points P_a , P_b , P_c and P_d marked in Fig. 8, we obtain values of 139.74, 140.23, 147.20 and 145.55 mmHg, respectively, for the case with 144 outlets and the corresponding values are 129.71, 131.29, 140.31 and 138.94 mmHg for the case with 18 outlets at $t = 1.2$ s. We see that discrepancies exist between the complex and simpler models in the pressure, as reported in Blanco et al. (2020). For the velocity, our interests focus on the pattern at $t = 1.4$ s during the late systole since it is more unstable comparing with that in the period of the early and mid systole, as reported in Youssefi et al. (2018). In Fig. 11, the instantaneous streamline of the velocity field and the velocities in cross sections for the two cases are presented. Generally speaking, both cases show some similar velocity fields, in which the streamline is relatively smooth near the inlet and become somehow complicated near the aneurysm and also near the bifurcation points. However, a careful comparison of the local blood flow pattern in the cross section shows the difference. In the cross sections of the right renal artery, even with the same value for

the organ resistance, the contour of the velocity is slightly changed and a lower value of the surface-averaged velocity 28.77 cm/s is obtained in the case of 144 outlets comparing to 30.99 cm/s in the case of 18 outlets. In the cross sections of the abdominal aorta, a significant difference is observed in the contours of the velocity and the slice-averaged velocities are 17.75 cm/s and 16.91 cm/s in the 144-outlets and 18-outlets cases, respectively. The smooth contours of the velocity in the cross sections show that the mesh is sufficient for this velocity field in the branches. In Fig. 12, we plot the

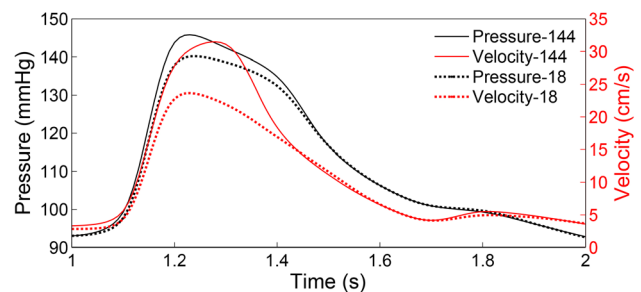


Fig. 12 The temporal variation of the averaged pressure and velocity over the abdominal slices in Fig. 11 for the cases of 144 and 18 outlets. “Pressure-144” and “Velocity-144” represent the case of 144 outlets. “Pressure-18” and “Velocity-18” represent the case of 18 outlets

temporal changes of the averaged pressure and velocity over the abdominal slices shown in Fig. 11 for the 144-outlets and 18-outlets cases. From the velocity profiles, we observe a change in the blood volume that goes through the cross section of the abdominal aorta. Overall, the peripheral branches affects the blood flow field both in time and in space. In this context, as discussed in Blanco et al. (2020), the complex arterial network has an advantage of reducing the impact of model assumption comparing to the simpler model.

3.4 Parallel scalability and solution sensitivity

In this subsection, we first study the parallel performance of the proposed algorithm. We then investigate the solution sensitivity with respect to the mesh size and the time-step size. Moreover, we examine the robustness of the proposed algorithm with respect to the terminal parameters, namely the total resistance R_T and capacitance C_T , which, if not specifically indicated, take the values $2680.97 \text{ dyn} \cdot \text{s}/\text{cm}^5$ and $4.16 \times 10^{-4} \text{ cm}^5/\text{dyn}$, respectively.

Table 5 shows the strong scalability of our solver tested on three meshes with 6.77×10^6 , 1.30×10^7 and 2.27×10^7 elements. The results are collected based on the first 20 time steps. In this table, “ np ” is the number of processor cores. “Newton” and “Time” are the average number of Newton iterations and the wall clock time for each time step, respectively. “GMRES” is the average number of linear iterations for each Newton step. “Speedup” and “Efficiency” are the speedup ratio and the parallel efficiency of our algorithm, which supposed to follow a linear growth with the increase in the number of processor cores. For each mesh, as the number of processor cores increases, we observe that the number of Newton iterations stays nearly as a constant, the number of GMRES changes gradually and the “Time”

decreases significantly. We obtain a parallel efficiency of 68% with 1200 cores, 74% with 1800 cores and 66% with 3000 cores for the three meshes from coarse to fine. To see it more clearly, the speedup and efficiency vs. the number of processors are plotted in Fig. 13. Thus, we conclude that our algorithm achieves good strong scalability with up to 3000 processor cores. Table 6 shows the weak scalability tested on meshes with 3.32×10^6 , 6.77×10^6 , 1.30×10^7 and 2.27×10^7 elements using 360, 720, 1440 and 2880 processor cores, respectively. The results show that the algorithm is not weakly scalable, for which the computing time should remain as a constant since the problem size on each processor is fixed. In Yang and Cai (2011), the authors indicate that a multilevel restricted additive Schwarz preconditioner may improve the weak scalability.

As shown in Table 7, we calculate the space-averaged pressure and velocity, and the flow rate for the four considered organs at $t = 0.2 \text{ s}$ and $t = 0.4 \text{ s}$, based on the three unstructured finite element meshes with 3.32×10^6 , 6.77×10^6 and 1.30×10^7 elements. We calculate the averaged quantities since the adopted meshes are unstructured and not uniformly refined. It shows that the accuracy of the space-averaged pressure and velocity is both improved with the increase in the number of elements, but the increment is small. Therefore, the mesh with 6.77×10^6 elements is adopted in the following tests as it balances the computational cost and the solution accuracy. It is noted that the instantaneous flow rate does not change much for the three meshes. We calculate the blood flow fraction based on the mesh with 6.77×10^6 elements and obtain values of 6.29% for the liver, 3.00% for the spleen, 9.43% and 9.02% for the left and right kidneys, respectively. The results are almost identical to the results calculated using the mesh with 1.43×10^7 elements in the previous section.

Table 5 Strong scalability tests for three meshes with 6.77×10^6 , 1.30×10^7 and 2.27×10^7 elements

Mesh	np	Newton	GMRES	Time (s)	Speedup	Efficiency
6.77×10^6	240	2.6	153.60	64.19	1.00	100%
	480	2.6	144.65	32.86	1.95	98%
	720	2.6	171.44	26.71	2.40	80%
	960	2.6	180.38	21.63	2.97	74%
	1200	2.6	180.94	18.84	3.41	68%
1.30×10^7	360	2.6	220.47	108.97	1.00	100%
	720	2.6	203.29	54.18	2.01	101%
	1080	2.5	242.74	43.36	2.51	84%
	1440	2.5	274.71	36.54	2.93	75%
	1800	2.5	256.14	29.54	3.69	74%
2.27×10^7	600	2.7	363.93	208.84	1.00	100%
	1200	2.7	390.83	119.55	1.75	87%
	1800	2.7	393.75	82.36	2.54	85%
	2400	2.7	444.53	74.32	2.81	70%
	3000	2.7	470.83	63.53	3.29	66%

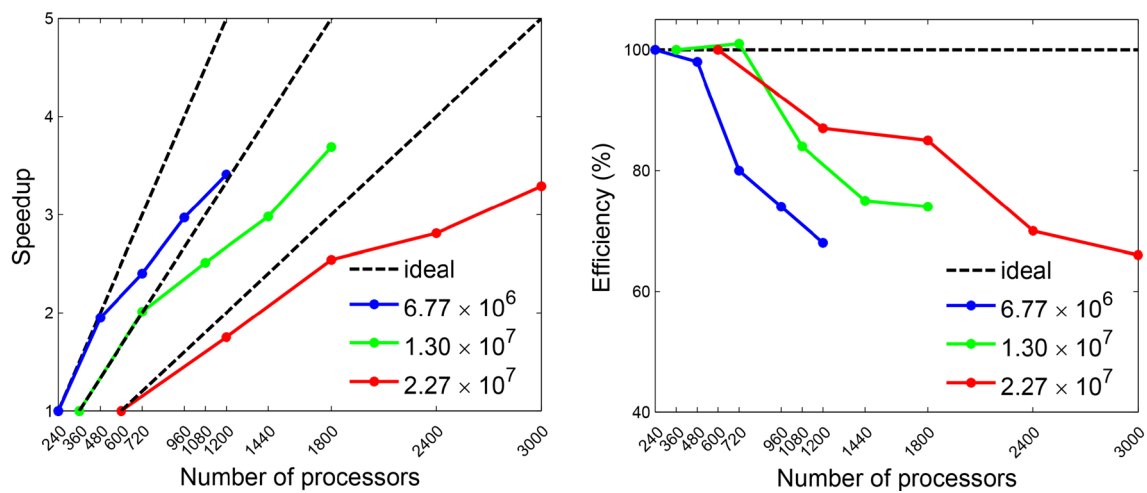


Fig. 13 The speedup and efficiency vs. the number of processors for three meshes with 6.77×10^6 , 1.30×10^7 and 2.27×10^7 elements. The black dash lines are for the ideal linear speedup with 100% efficiency

Table 6 Weak scalability tested on meshes with 3.32×10^6 , 6.77×10^6 , 1.30×10^7 and 2.27×10^7 elements using 360, 720, 1440 and 2880 processor cores, respectively

Mesh	np	Newton	GMRES	Time (s)
3.32×10^6	360	2.3	158.54	20.71
6.77×10^6	720	2.6	171.44	26.71
1.30×10^7	1440	2.5	274.71	36.54
2.27×10^7	2880	2.6	465.44	62.48

This demonstrates that our computed blood flow fraction is mesh-independent.

The time-step size influences the convergence of the numerical algorithm as well as the accuracy of the solution. Our algorithm is not restricted by the CFL condition owing to the fully implicit temporal scheme. In Table 8, we study the solution sensitivity with respect to the time-step sizes 5×10^{-4} , 1×10^{-3} and 2×10^{-3} . It can be seen that the algorithm converges for all time step sizes. The decrease in the time-step size improves the solution accuracy, but increases

Table 7 The space-averaged pressure (mmHg) and magnitude of velocity (cm/s), and the flow rate (ml/s) to interested organs at $t = 0.2$ s and 0.4 s obtained using meshes with different number of elements

Mesh	Pressure $t=0.2$ s	Pressure $t=0.4$ s	Velocity $t=0.2$ s	Velocity $t=0.4$ s	Flow rate $t=0.2$ s				Flow rate $t=0.4$ s			
					liver / spleen / left & right kidney				liver / spleen / left & right kidney			
3.32×10^6	145.68	136.40	44.53	13.92	16.75 / 9.98 / 21.77 / 15.71	6.14 / 2.53 / 7.66 / 8.08						
6.77×10^6	144.04	135.97	44.28	13.93	17.08 / 9.88 / 21.73 / 15.86	5.96 / 2.53 / 7.69 / 8.13						
1.30×10^7	143.04	135.88	44.12	13.89	17.39 / 9.89 / 21.80 / 16.03	5.93 / 2.56 / 7.69 / 8.15						

Table 8 The space-averaged pressure (mmHg) and magnitude of velocity (cm/s), and the flow rate (ml/s) to interested organs at $t = 0.2$ s and 0.4 s obtained with different time-step sizes

Time-step sizes	Pressure $t=0.2$ s	Pressure $t=0.4$ s	Velocity $t=0.2$ s	Velocity $t=0.4$ s	Flow rate $t=0.2$ s				Flow rate $t=0.4$ s			
					liver / spleen / left & right kidney				liver / spleen / left & right kidney			
5×10^{-4}	143.46	135.92	44.41	13.88	17.17 / 9.87 / 21.68 / 15.83	5.95 / 2.56 / 7.76 / 8.19						
1×10^{-3}	144.04	135.97	44.28	13.93	17.08 / 9.88 / 21.73 / 15.86	5.96 / 2.53 / 7.69 / 8.13						
2×10^{-3}	144.67	136.07	44.09	13.91	17.05 / 9.91 / 21.80 / 15.91	5.93 / 2.50 / 7.62 / 8.10						

Table 9 The robustness of the algorithm with respect to the total resistance R_T and the total capacitance C_T

R_T (dyn · s/cm ⁵)	Newton	GMRES	Time (s)
1340.49	2.6	133.49	30.87
2680.97	2.6	144.65	32.86
5361.94	2.6	166.75	36.23
C_T (cm ⁵ /dyn)			
2.08×10^{-4}	2.6	154.31	34.92
4.16×10^{-4}	2.6	144.65	32.86
8.32×10^{-4}	2.6	137.29	31.48

the number of iterations and affects the overall execution time. Therefore, the time-step size 1×10^{-3} is adopted in this work after considering the computing time vs. accuracy.

Table 9 shows the robustness of the algorithm with respect to the terminal parameters, including the total resistance R_T and the total capacitance C_T . By using 480 processor cores, R_T with values 1340.49, 2680.97 and 5361.94 and C_T with values 2.08×10^{-4} , 4.16×10^{-4} and 8.32×10^{-4} are tested. It can be seen that the number of nonlinear iterations stays at 2.6 for all the tests. The increase in the value of R_T leads to a small increase in GMRES iterations and the averaged computing time as well. The increase in the value of C_T slightly decreases the GMRES iterations and reduces the computing time. Overall, the proposed algorithm is robust with respect to both R_T and C_T .

3.5 Limitation

The rigid wall assumption is a potential limitation of this study. However, although the fluid-structure interaction (FSI) may have some influences on the pressure and velocity patterns, it should not have a strong impact on the distribution of the blood flow (Lopes et al. 2019). Moreover, it is very difficult to obtain the patient-specific thickness and material properties of the artery wall. Without the correct geometry and material parameters, the results from the FSI computation may actually be worse than the fluid only simulations.

4 Concluding remarks

In this paper, we studied a highly parallel algorithm for the simulation of blood flows in the abdominal aorta with all primary organs and 144 branches. The 3-element Windkessel model was applied to all the outlets, and a two-level organ-based resistance splitting method was introduced. We validated the proposed approach by comparing the result with that obtained with a commercial software package ANSYS CFX. Since the blood supply to specific organs is regulated

by the terminal resistance, we therefore predetermine their values by a resistance-flow relationship. This procedure requires no additional computational cost and produces physiologically correct results. Our numerical experiments show that local hemodynamic properties depend on the artery used in the simulation. Keeping more branches of the arterial network increases the computational cost, but brings refined blood flow patterns comparing to the coarser anatomical model. We also investigated the solution accuracy in terms of the mesh size and the time-step size and studied the parallel scalability of the proposed algorithm. In summary, the proposed parallel algorithm is capable of solving blood flow simulation problems in patient-specific arteries with a complex network of arterial branches. The method will potentially be useful for surgical planning involving the organs receiving blood from the abdominal aorta.

Acknowledgements This work was partially supported by the National Key R&D Program of China (Grant No. 2016YFB0200601), the National Natural Science Foundation of China (Grant Nos. 11801543 and 81871447) and the Shenzhen grants (Grant Nos. ZDSYS201703031711426, JCYJ20190806165805433 and SZBL2019062801002).

References

- Ambler G, Coughlin P, Hayes P, Varty K, Gohel M, Boyle J (2015) Incidence and outcomes of severe renal impairment following ruptured abdominal aortic aneurysm repair. *Eur J Vasc Endovasc Surg* 50(4):443–449
- Balay S, Abhyankar S, Adams MF, Brown J, Brune P, Buschelman K, Dalcin L, Dener A, Eijkhout V, Gropp W et al. (2020) PETSc Users Manual revision 3.13. Technical report, Argonne National Lab.(ANL), Argonne, IL
- Barker AT, Cai X-C (2010) Scalable parallel methods for monolithic coupling in fluid-structure interaction with application to blood flow modeling. *J Comput Phys* 229(3):642–659
- Blanco P, Watanabe S, Feijóo R (2012) Identification of vascular territory resistances in one-dimensional hemodynamics simulations. *J Biomech* 45(12):2066–2073
- Blanco PJ, Müller LO, Watanabe SM, Feijóo RA (2020) On the anatomical definition of arterial networks in blood flow simulations: comparison of detailed and simplified models. *Biomech Model Mechan* 19(5):1663–1678
- Blanco PJ, Watanabe SM, Dari EA, Passos MAR, Feijóo RA (2014) Blood flow distribution in an anatomically detailed arterial network model: criteria and algorithms. *Biomech Model Mechan* 13(6):1303–1330
- Boyd AJ, Kuhn DC, Lozowy RJ, Kulbisky GP (2016) Low wall shear stress predominates at sites of abdominal aortic aneurysm rupture. *J Vasc Surg* 63(6):1613–1619
- Capoccia M (2015) Development and characterization of the arterial windkessel and its role during left ventricular assist device assistance. *Artif Organs* 39(8):E138–E153
- Chaikof EL, Dalman RL, Eskandari MK, Jackson BM, Lee WA, Mansour MA, Mastracci TM, Mell M, Murad MH, Nguyen LL et al (2018) The society for vascular surgery practice guidelines on

- the care of patients with an abdominal aortic aneurysm. *J Vasc Surg* 67(1):2–77
- Chisci E, Alamanni N, Iacoponi F, Michelagnoli S, Procacci T, Colombo G, Setacci C (2018) Grading abdominal aortic aneurysm rupture risk. *J Card Surg* 59(1):87–94
- Chung B, Cebal JR (2015) CFD for evaluation and treatment planning of aneurysms: review of proposed clinical uses and their challenges. *Ann Biomed Eng* 43(1):122–138
- Figueroa CA, Humphrey JD (2014) Pressure wave propagation in full-body arterial models: a gateway to exploring aging and hypertension. *Procedia IUTAM* 10:382–395
- Fossan FE, Sturdy J, Müller LO, Strand A, Bråten AT, Jørgensen A, Wiseth R, Hellevik LR (2018) Uncertainty quantification and sensitivity analysis for computational FFR estimation in stable coronary artery disease. *Cardiovasc Eng Techn* 9(4):597–622
- Frauenfelder T, Lotfey M, Boehm T, Wildermuth S (2006) Computational fluid dynamics: hemodynamic changes in abdominal aortic aneurysm after stent-graft implantation. *Cardiovasc Inter Rad* 29(4):613–623
- Ghulam Q, Bredahl K, Lönn L, Rouet L, Sillesen H, Eiberg J (2017) Follow-up on small abdominal aortic aneurysms using three dimensional ultrasound: volume versus diameter. *Eur J Vasc Endovasc Surg* 54:439–445
- Grinberg L, Anor T, Madsen J, Yakhot A, Karniadakis G (2009) Large-scale simulation of the human arterial tree. *Clin Exp Pharmacol Physiol* 36(2):194–205
- Grinberg L, Karniadakis GE (2008) Outflow boundary conditions for arterial networks with multiple outlets. *Ann Biomech Eng* 36(9):1496–1514
- Kandail H, Hamady M, Xu XY (2015) Comparison of blood flow in branched and fenestrated stent-grafts for endovascular repair of abdominal aortic aneurysms. *J Endovasc Ther* 22(4):578–590
- Keegan J, Patel HC, Simpson RM, Mohiaddin RH, Firmin DN (2015) Inter-study reproducibility of interleaved spiral phase velocity mapping of renal artery haemodynamics. *J Cardiovasc Magn Reson* 17(1):8
- Kent KC (2014) Abdominal aortic aneurysms. *N Engl J Med* 371(22):2101–2108
- Kong F, Kheyfets V, Finol E, Cai X-C (2018) An efficient parallel simulation of unsteady blood flows in patient-specific pulmonary artery. *Int J Numer Meth Bio* 34(4):e2952
- Lan H, Updegrave A, Wilson NM, Maher GD, Shadden SC, Marsden AL (2018) A re-engineered software interface and workflow for the open-source Simvascular cardiovascular modeling package. *J Biomech Eng* 140(2):024501
- Lee D, Chen J (2002) Numerical simulation of steady flow fields in a model of abdominal aorta with its peripheral branches. *J Biomech* 35(8):1115–1122
- Lee D, Chen J (2003) Pulsatile flow fields in a model of abdominal aorta with its peripheral branches. *Biomed Eng Appl Basis Commun* 15(05):170–178
- Lefferts WK, Augustine JA, Heffernan KS (2014) Effect of acute resistance exercise on carotid artery stiffness and cerebral blood flow pulsatility. *Front Physiol* 5:101
- Les AS, Shadden SC, Figueroa CA, Park JM, Tedesco MM, Herfkens RJ, Dalman RL, Taylor CA (2010) Quantification of hemodynamics in abdominal aortic aneurysms during rest and exercise using magnetic resonance imaging and computational fluid dynamics. *Ann Biomed Eng* 38(4):1288–1313
- Li Z, Jiang W, Yuan D, Chen Y, Tian X, Zhou Z (2018) Investigation of the hemodynamics of a juxtarenal aortic aneurysm with intervention by dual-stents strategy. *Clin Biomech* 58:109–115
- Liao Z-J, Chen R, Yan Z, Cai X-C (2019) A parallel implicit domain decomposition algorithm for the large eddy simulation of incompressible turbulent flows on 3D unstructured meshes. *Int J Numer Meth Fl* 89(9):343–361
- Liu H, Liang F, Wong J, Fujiwara T, Ye W, Tsubota K-I, Sugawara M (2015) Multi-scale modeling of hemodynamics in the cardiovascular system. *Acta Mech Sin* 31(4):446–464
- Liu J, Yan Z, Pu Y, Shiu W-S, Wu J, Chen R, Leng X, Qin H, Liu X, Jia B et al (2017) Functional assessment of cerebral artery stenosis: a pilot study based on computational fluid dynamics. *J Cereb Blood Flow Metab* 37(7):2567–2576
- Lopes D, Puga H, Teixeira J, Teixeira S (2019) Influence of arterial mechanical properties on carotid blood flow: comparison of CFD and FSI studies. *Int J Mech Sci* 160:209–218
- Luo L, Shiu W-S, Chen R, Cai X-C (2019) A nonlinear elimination preconditioned inexact newton method for blood flow problems in human artery with stenosis. *J Comput Phys* 399:108926
- Morris PD, Narracott A, von Tengg-Kobligk H, Soto DAS, Hsiao S, Lungu A, Evans P, Bressloff NW, Lawford PV, Hose DR et al (2016) Computational fluid dynamics modelling in cardiovascular medicine. *Heart* 102(1):18–28
- Nakamura T, Moriyasu F, Ban N, Nishida O, Tamada T, Kawasaki T, Sakai M, Uchino H (1989) Quantitative measurement of abdominal arterial blood flow using image-directed doppler ultrasonography: superior mesenteric, splenic, and common hepatic arterial blood flow in normal adults. *J Clin Ultrasound* 17(4):261–268
- Owen B, Lowe C, Ashton N, Mandal P, Rogers S, Wein W, McCollum C, Revell A (2016) Computational hemodynamics of abdominal aortic aneurysms: three-dimensional ultrasound versus computed tomography. *Proc Inst Mech Eng H* 230(3):201–210
- Regnier P, Lareyre F, Hassen-Khodja R, Durand M, Touma J, Raffort J (2018) Sexual dysfunction after abdominal aortic aneurysm surgical repair: current knowledge and future directions. *Eur J Vasc Endovasc Surg* 55(2):267–280
- Sato S, Ohnishi K, Sugita S, Okuda K (1987) Splenic artery and superior mesenteric artery blood flow: nonsurgical Doppler measurement in healthy subjects and patients with chronic liver disease. *Radiology* 164(2):347–352
- Shipkowitz T, Rodgers V, Frazin LJ, Chandran K (1998) Numerical study on the effect of steady axial flow development in the human aorta on local shear stresses in abdominal aortic branches. *J Biomech* 31(11):995–1007
- Shipkowitz T, Rodgers V, Frazin LJ, Chandran K (2000) Numerical study on the effect of secondary flow in the human aorta on local shear stresses in abdominal aortic branches. *J Biomech* 33(6):717–728
- Taylor CA, Fonte TA, Min JK (2013) Computational fluid dynamics applied to cardiac computed tomography for noninvasive quantification of fractional flow reserve: scientific basis. *J Am Coll Cardiol* 61(22):2233–2241
- Taylor CA, Hughes TJ, Zarins CK (1998) Finite element modeling of three-dimensional pulsatile flow in the abdominal aorta: relevance to atherosclerosis. *Ann Biomed Eng* 26(6):975–987
- Tse KM, Chiu P, Lee HP, Ho P (2011) Investigation of hemodynamics in the development of dissecting aneurysm within patient-specific dissecting aneurysmal aortas using computational fluid dynamics (CFD) simulations. *J Biomech* 44(5):827–836
- Valentin J (2002) Basic anatomical and physiological data for use in radiological protection: reference values. *Ann ICRP* 32(3–4):1–277
- Vignon-Clementel IE, Figueroa CA, Jansen KE, Taylor CA (2006) Outflow boundary conditions for three-dimensional finite element modeling of blood flow and pressure in arteries. *Comput Methods Appl Mech Eng* 195(29–32):3776–3796
- Xiao N (2014) Simulation of 3-D blood flow in the full systemic arterial tree and computational frameworks for efficient parameter estimation. PhD thesis, Stanford University

- Xiao N, Alastruey J, Alberto Figueroa C (2014) A systematic comparison between 1-D and 3-D hemodynamics in compliant arterial models. *Int J Numer Meth Bio* 30(2):204–231
- Xiong Y, Wang X, Jiang W, Tian X, Wang Q, Fan Y, Chen Y (2016) Hemodynamics study of a multilayer stent for the treatment of aneurysms. *Biomed Eng online* 15(2):134
- Yang C, Cai X-C (2011) Parallel multilevel methods for implicit solution of shallow water equations with nonsmooth topography on the cubed-sphere. *J Comput Phys* 230(7):2523–2539
- Yang C, Cai X-C (2014) A scalable fully implicit compressible Euler solver for mesoscale nonhydrostatic simulation of atmospheric flows. *SIAM J Sci Comput* 36(5):S23–S47
- Youssefi P, Gomez A, Arthurs C, Sharma R, Jahangiri M, Alberto Figueroa C (2018) Impact of patient-specific inflow velocity profile on hemodynamics of the thoracic aorta. *J Biomech Eng* 140(1):011002
- Yzet T, Bouzerar R, Allart J-D, Demuynck F, Legallais C, Robert B, Deramond H, Meyer M-E, Balédent O (2010) Hepatic vascular flow measurements by phase contrast MRI and Doppler echography: a comparative and reproducibility study. *J Magn Reson Imaging* 31(3):579–588
- Zhang J, Critchley L, Huang L (2015) Five algorithms that calculate cardiac output from the arterial waveform: a comparison with Doppler ultrasound. *Brit J Anaesth* 115(3):392–402
- Zhang R, Behbehani K, Levine BD (2009) Dynamic pressure-flow relationship of the cerebral circulation during acute increase in arterial pressure. *J physiol* 587(11):2567–2577
- Zhou M, Sahni O, Kim HJ, Figueroa CA, Taylor CA, Shephard MS, Jansen KE (2010) Cardiovascular flow simulation at extreme scale. *Comput Mech* 46(1):71–82
- Zhou S, Xu L, Hao L, Xiao H, Yao Y, Qi L, Yao Y (2019) A review on low-dimensional physics-based models of systemic arteries: application to estimation of central aortic pressure. *Biomed Eng Online* 18(1):41

Publisher's Note Springer Nature remains neutral with regard to jurisdictional claims in published maps and institutional affiliations.